# Probing the Electronic Structure of Small Molecular Anions by Photoelectron Imaging†

**Eric Surber, Richard Mabbs, and Andrei Sanov***

*Department of Chemistry, University of Arizona, Tucson, Arizona 85721-0041*

*Received: December 27, 2002; In Final Form: April 18, 2003*

We outline the methodology of negative-ion photoelectron imaging and general aspects of interpretation of the results using the $CS_2^-$ and $S_2^-$ anions as model systems. The $CS_2^-$ images are recorded using 800, 530, 400, and 267 nm photons. The observed transitions result in the formation of $CS_2$ in the X $^1\Sigma_g^+$, a $^3B_2$, b $^3A_2$, and A $^1A_2$ states. The $S_2^-$ measurements are carried out at the same wavelengths with the exception of 800 nm. The resulting images reveal the detachment transitions assigned to the X $^3\Sigma_g^-$, a $^1\Delta_g$, b $^1\Sigma_g^+$, c $^1\Sigma_u^-$, and A′ $^3\Delta_u$ states of the neutral. The choice of detachment wavelengths serves as a "zoom" selectively focusing on chosen transitions, in some cases allowing the observation of their vibrational structure. The photoelectron spectra and angular distributions obtained from the images are used to discuss the electronic structure and detachment dynamics. In particular, two approaches to interpreting the angular distributions are discussed. One method employs the Cooper−Zare central-potential model adapted to the molecular case. It considers an expansion of the parent orbital in the basis of single-center atomic-orbital functions, for which the partial waves comprising the ejected electron are determined. The application of this model to molecular anions is straightforward, if the parent molecular orbital resembles an atomic orbital, which is the case for $S_2^-$, but not $CS_2^-$. In the latter case, a different qualitative approach is proposed, which (i) relies upon the electric-dipole approximation and group theory for the determination of the detached electron wave function symmetry, (ii) restricts the analysis to symmetry (electric dipole) allowed s and p partial waves, and (iii) qualitatively treats the orientation averaging by considering only a few "principal" molecular orientations. The results provide a foundation for the qualitative interpretation of anion photoelectron images.

## 1. Introduction

Photoelectron imaging of negative ions has emerged as a novel approach to the studies of electronic structure and dynamics, complementing traditional photoelectron spectroscopy with a heightened emphasis on the electronic wave functions. The conceptually straightforward technique provides maps of the electron detachment process, including the interdependent angular and kinetic energy distributions. The two-dimensional measurement in space of both observables is highly instrumental in the determination of molecular structure and electronic wave function symmetry. The application of these imaging capabilities in the time domain promises new insights into chemical dynamics as viewed from the electronic perspective.[1−5]

The original application of imaging to gas-phase dynamics by Houston and Chandler involved neutral photofragments tagged by state-selective laser ionization.[6] In recent years, both the photofragment-ion and photoelectron variants of imaging received boosts from the improvements in experimental technology and methodology. In particular, velocity mapping introduced by Eppink and Parker[7,8] revolutionalized the field by decreasing image blurring and hence drastically improving the resolution. This and other developments[9−11] have increased the level of detail obtainable by imaging, making the technique more versatile and powerful in the studies of gas-phase interactions.

As with photofragment-ion imaging, photoelectron imaging was initially implemented for neutral molecules. Several benchmark studies demonstrated the utility of energy and time-resolved photoelectron angular distributions (PAD) in the studies of structure and time-resolved dynamics.[2,4] On the other hand, very few photoelectron imaging experiments involving molecular negative ions have been reported to date.[12,13] In this paper, we demonstrate the capabilities of our new instrument in probing the electronic structure of negative ions by photoelectron imaging. We present the results for two small molecular anions, $S_2^-$ and $CS_2^-$, which are used as model systems highlighting general aspects of the methodology behind the experimental collection and analysis of anion photoelectron images.

The information content of photoelectron images differs from their photofragment-ion counterparts. While the velocity (speed) distributions of the photofragments and photoelectrons both reflect the energetics of the reaction or electron emission process, the corresponding angular distributions may have different meanings. Therefore, the two types of imaging can provide complementary insights into molecular structure and reaction dynamics.

In the elementary case of prompt dissociation via a single transition, the photofragment anisotropy can be understood in terms of preferential excitation of those molecules whose transition dipole moments are aligned along the laser polarization axis.[14,15] In the semiclassical picture, the angular distribution of the photofragments in the molecular frame (MF) is determined by the arrangement of chemical bonds and the direction of forces during dissociation. For example, in the dissociation of a nonrotating diatomic with the fragment repulsion directed along the internuclear axis, the MF angular distribution is (classically) a delta function peaking in the direction of the bond.[16] It transforms into a cosine-squared or a sine-squared distribution of recoil angles with respect to the laser polarization

† Part of the special issue "A. C. Albrecht Memorial Issue".

* Corresponding author. E-mail: sanov@u.arizona.edu.

10.1021/jp027838o CCC: $25.00 
Published on Web 06/07/2003

in the laboratory frame (LF), depending on the parallel or perpendicular nature of the transition.

However, this picture is applicable only if the electronic transition is either purely parallel or purely perpendicular, which is rather the exception than the rule. More commonly, the recoil anisotropy is governed by the competition of transition dipole moments of different symmetry, as well as the dissociation dynamics.[14,16−20] The information content of photofragment angular distributions is further enriched by the effect of molecular rotation on the time scale of dissociation. Rotation reduces the observed anisotropy, providing a way to estimate a finite dissociation lifetime.[21−23] Thus, photofragment angular distributions can help distinguish between reaction mechanisms, e.g., direct dissociation or unimolecular decomposition.[24]

In photodetachment, the photoelectron anisotropy (or lack thereof) can also signal a distinction between direct and indirect pathways. For example, isotropic PADs are characteristic of autodetachment and cluster thermionic emission.[25−28] However, in direct photodetachment electron ejection is usually fast compared to molecular rotation and, at least within the Born−Oppenheimer picture, the PAD has no bearing on the electron detachment time scale.

Even in the most straightforward cases, the PADs observed by photoelectron imaging can be understood only in quantum terms. In the case of molecular anions, different components of the transition dipole moment yield series of free-electron waves specific to the transition. In the single-center partial-wave expansion model, the photodetachment process is governed not only by moduli of the transition moments but also by relative phases between them. As a result, the MF PADs, which are related to the angular parts of the free-electron wave functions, can have very complex structures.[29]

There have been experiments probing the molecule-fixed PADs arising from negative ions, such as the photoelectron−photofragment coincidence measurements by Continetti and co-workers.[30,31] This paper is concerned with photoelectron imaging restricted to the laboratory frame, in which averaging over molecular orientations renders the PADs misleadingly simple bipolar structures. In fact, the LF photoelectron distributions produced by linearly polarized light have the same form as photofragment angular distributions.[14,32,33] However, the interpretation of the PADs involves deciphering their relation to the complex molecular-frame free-electron wave function. Assuming a one-electron approximation, the latter is a signature of the precursor molecular orbital (MO), as well as the photodetachment process. The analysis is, in general, much less intuitive than the semiclassical model applicable to the simplest photofragmentation cases.

Theoretical treatments of both direct and time-dependent angle-resolved ionization of neutral molecules have been under development for over 30 years.[29,32−39] As with experimental work, fewer theoretical studies specifically targeted PADs in the photodetachment of molecular anions.[18,40] An important difference between neutral ionization and anion photodetachment lies in the scaling of partial cross sections with energy, defined by the different types of long-range potentials involved in the interaction of the electron with the positively charged versus neutral core.[41]

Amid the development of rigorous theoretical treatments, there remains a need for qualitative models describing the detachment processes and resulting PADs. The objective of these models is to provide basic understanding and tutorial description of electron-ejection dynamics without embarking on full-scale quantum calculations. Many ideas helping in understanding molecular anion photodetachment have been developed with regard to atomic anions,[42,43] as well as molecular anions with atomic-like MOs.[12,44,45] Other relevant ideas regarding the interference of partial waves have been discussed in the context of threshold photodetachment.[44,46,47]

The recent explosion of interest in photoelectron imaging prompts us to revisit these ideas and adapt them to the current needs of experimentalists working in the field. In this paper, we use $S_2^-$ and $CS_2^-$ as model systems and, drawing on the wealth of available knowledge, discuss practical and visual approaches to decoding the information contained in the images.

The two qualitative models that we employ are based on the formalism originally developed for describing not only PADs, but also near-threshold behaviors. The first is an extension of the central-potential model for atomic ionization and photodetachment.[33] As discussed by Cooper and Zare, it can be generalized to the molecular anion case,[32] but such generalization yields useful qualitative insights only if the parent MO resembles an atomic orbital (AO).[45] Formally, this model considers an expansion of the MO in the basis of single-center AO functions, for which the partial waves of the ejected electron can be determined. We test the performance of this model on $S_2^-$ imaging data and use it as a steppingstone to tackling more complex systems.

For photodetachment from MOs that cannot be conveniently approximated by a single AO (exemplified here by $CS_2^-$), another qualitative approach is suggested, applying specifically to molecular negative ions. The model restricts the analysis to s and p partial waves, relying on the approximate Wigner threshold law for anion photodetachment.[41,48] The MF → LF transformation and orientation averaging are accounted for qualitatively by considering only a few "principal" molecular orientations.

The results for $CS_2^-$ presented here expand on our previous communication,[13] while the $S_2^-$ results are presented for the first time. While this is the first photoelectron imaging study of both anions, traditional photoelectron spectroscopy has been applied to them previously. In particular, a $CS_2^-$ photoelectron spectrum[49,50] taken with 2.54 eV photons revealed a single electronic transition assigned to the X $^1\Sigma_g^+$ state of the neutral. A higher photon energy (4.66 eV) spectrum recorded by Tsukuda et al.[51] showed additional peaks assigned to the a $^3B_2$, b $^3A_2$, and A $^1A_2$ neutral states. The comparison of the latter spectrum to the present results is particularly revealing in demonstrating the capabilities of photoelectron imaging. A 2.54 eV photoelectron spectrum of $S_2^-$ was obtained by Ellison and co-workers,[52] revealing a vibrational progression assigned to the X $^3\Sigma_g^-$ state of $S_2$. We report a series of $S_2^-$ photoelectron images recorded in the photon energy range between 2.34 and 4.64 eV, which reveal the structure of the detachment transitions assigned to the X $^3\Sigma_g^-$, a $^1\Delta_g$, b $^1\Sigma_g^+$, c $^1\Sigma_u^-$, and A′ $^3\Delta_u$ states of the neutral.

This paper is organized as follows. Section 2 gives a description of the experimental apparatus used in the study. Section 3 presents the experimental results and analysis. The implications of the results and the qualitative models employed for the interpretation of photoelectron images are discussed in section 4. A brief summary is given in section 5.

## 2. Experimental Apparatus

The negative-ion photoelectron imaging spectrometer employed in this study is shown schematically in Figure 1. It consists of a pulsed ion source,[53] a Wiley−McLaren[54] time-of-flight mass spectrometer,[53,55] and a velocity-map[7] photoelectron

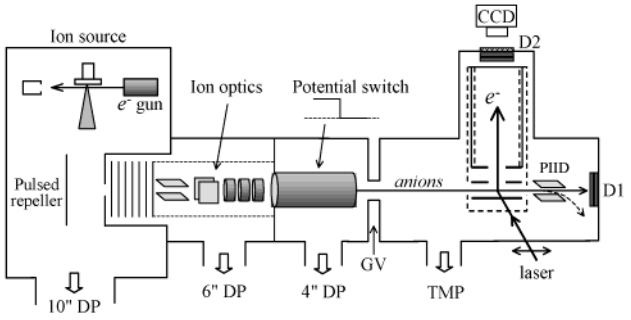


**Figure 1.** Schematic diagram of the negative-ion photoelectron imaging spectrometer. DP, diffusion pump; TMP, turbomolecular pump; GV, gate valve; PIID, postimaging ion deflector; D1, ion/neutral detector; D2, photoelectron imaging detector. Double-headed arrow crossing the laser beam indicates the laser polarization direction.

imaging assembly. In the previous communication,[13] we made only brief reference to the whole apparatus, although a more detailed description of the mass spectrometer has been given elsewhere.[55]

The negative ions are generated and mass analyzed using the state-of-art techniques pioneered by Lineberger and co-workers.[53,56] The ions are formed by secondary electron attachment in an electron-impact ionized pulsed supersonic expansion of a precursor gas mixture. In this work, $CS_2^-$ ions are prepared by expanding carbon disulfide (ambient vapor pressure) seeded in 3 atm of Ar. The $S_2^-$ ions are made from a 5−10% mixture of carbonyl sulfide in Ar at a backing pressure of 1.5−2 atm. The gas mixture is expanded into the source chamber with a base pressure of $10^{-6}$ Torr through a General Valve Series 9 nozzle operated at a repetition rate of 30−50 Hz. The beam of electrons from a 1 keV electron gun crosses the supersonic expansion 1−2 mm from the 500 $\mu$m diameter orifice of the nozzle.

About 15 cm downstream from the nozzle, the anions are pulse-extracted into the 1.7 m long Wiley−McLaren time-of-flight mass spectrometer. A 10 ns rise/fall time high-voltage pulse generator (Directed Energy PVM-4210) drives the repeller plate. The amplitude of the extraction pulse is adjusted for optimum Wiley−McLaren focusing, the typical value being about −600 V. The ions pass through a 4 mm diameter orifice in the grounded electrode (which also serves as a partition between the source chamber and the rest of the instrument) and enter the acceleration stack, where a uniform electric field from 10 evenly spaced electrodes accelerates them to the 1950 V beam potential.

The accelerated ions are steered and focused using electrostatic deflectors and an Einzel lens, collectively referred to as ion optics in Figure 1. Following that, the ions are referenced from the 1950 V beam potential down to the ground potential without affecting their kinetic energy using a fast potential switch, as described by Johnson and co-workers.[57] The switch is a 60 cm long, 7.5 cm diameter stainless steel tube with apertures at both ends, driven by a 25 ns rise/fall time high-voltage pulse generator (Directed Energy PVX-4140).

After passing through two differentially pumped regions and a series of apertures, the ions enter the detection chamber. The base pressure in this region is $\sim 2 \times 10^{-9}$ Torr, rising somewhat when the gate valve connecting it with the rest of the instrument is opened.

The ions are detected at the end of the flight tube using a Chevron-type dual microchannel plate (MCP) detector (D1 in Figure 1) with 25 mm diameter plates and a metal anode (Burle, Inc.). Before impacting the detector, the ions are postaccelerated by an additional 1 kV, raising their kinetic energy to >3 kV. The signal from the detector anode, floating on top of a high-voltage pedestal, is capacitively coupled down to the ground potential, amplified (100×), and monitored with a 300 MHz digital averaging oscilloscope (Tektronix TDS 3032). The anion masses are assigned using the established instrument calibration as well as the known spectral patterns.[55]

The postimaging ion deflector (PIID in Figure 1), located between the imaging assembly ion exit and detector D1, gives the option of deflecting the ions away from the instrument axis, enabling the detection of neutral photodetachment (and/or photodissociation) products. This capability is used for finding the overlap between laser pulses and the ion bunches of desired mass in the pulsed ion beam.

The photoelectrons detached from the mass-selected negative ions are analyzed using the imaging technique pioneered by Chandler and Houston,[6] implemented here in the velocity-mapping modification of Parker and Eppink.[7] The imaging assembly is comprised of a three-electrode lens and a 15 cm long field-free electron flight tube. The assembly is mounted vertically, with its axis perpendicular to the ion and laser beams (see Figure 1). The entire assembly, including the imaging lens, is encased within several layers of $\mu$-metal, shielding it from the Earth's magnetic field. The bottom part of the shield is kept at ground potential and has ~2 cm diameter apertures for the laser and ion beams. The field-free flight tube has two double-layer shields, both inside and outside the tube. The imaging lens consists of three 10 cm diameter oxygen-free high-conductivity copper electrodes, evenly spaced at 2.5 cm. The bottom element serves as repeller ($V_1 < 0$), the middle is at ground potential ($V_2 = 0$), and the top one serves as an accelerating element ($V_3 > 0$). The second and third electrodes have 2.5 cm diameter apertures at their centers. The accelerating element is physically and electrically connected to the field-free flight tube.

The collimated ion beam enters the imaging assembly through the outer shield aperture and passes between the repeller and ground electrodes. After exiting the assembly through the opposing shield aperture, the beam trajectory can be corrected, if needed, for the deflection due to the repeller field by applying an opposite-sign potential difference to the postimaging ion deflector (PIID).

The velocity-map focusing for the photodetached electrons is optimized by adjusting the absolute ratio of potentials $V_1$ and $V_3$ applied to the repeller and the accelerating element, respectively. The optimum ratio (1:3 for our experimental geometry) was determined by observing the narrow atomic photodetachment transitions in $I^-$ at 267 nm.[58] This ratio is maintained throughout all measurements, while $V_1$ and $V_3$ are varied in a coupled fashion in the range $V_3 = 150-750$ V, depending on characteristic electron kinetic energies (eKEs), to adjust the photoelectron flight time for efficient use of the imaging detector area.

The flight tube is terminated with a 333 lines per inch mesh mounted several millimeters away from the imaging MCP detector (D2 in Figure 1) input surface. After passing through the mesh, the photoelectrons are postaccelerated into the front MCP by an additional ~1 kV. The imaging detector (Burle, Inc.) includes two imaging quality 40 mm diameter MCPs and a P47 phosphor screen coupled to an outside chamber window by a fiber-optic bundle. To discriminate against noise, the MCPs are operated in a pulsed-bias mode, whereas the total bias across the two plates, normally kept at 1.0−1.2 V, is pulsed up to 1.6−1.8 kV for a 200−300 ns window timed to coincide with the arrival of the photoelectrons. The high-voltage pulses are

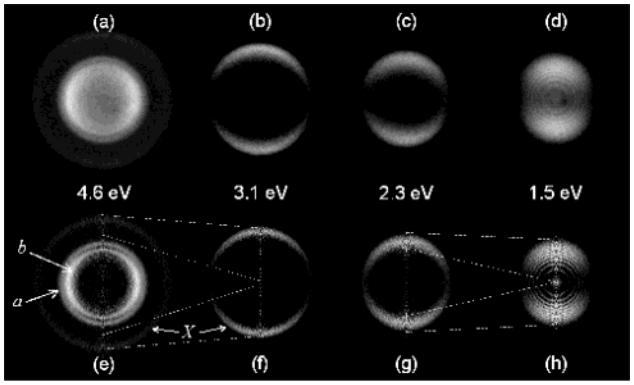


**Figure 2.** Top row: Photoelectron images recorded in the photodetachment of $CS_2^-$ at (a) 267, (b) 400, (c) 530, and (d) 800 nm, with the corresponding photon energies indicated. Bottom row: Abel inversions of the above images, reconstructed as described in the text. The images are shown on arbitrary velocity and intensity scales; see Figures 4 and 5 and the text for quantitative information. The laser polarization is always vertical in the figure plane. Arrows labeled *X*, *a*, and *b* indicate transitions accessing the X $^1\Sigma_g^+$, a $^3B_2$, and b $^3A_2$ states of neutral $CS_2$. The transition to the A $^1A_2$ state (not labeled) is just inside the b $^3A_2$ ring in (e), as discussed in the text and seen in Figure 4. The dashed lines show correlations in the velocity-map domain of the selected eBE intervals between images taken at different wavelengths.

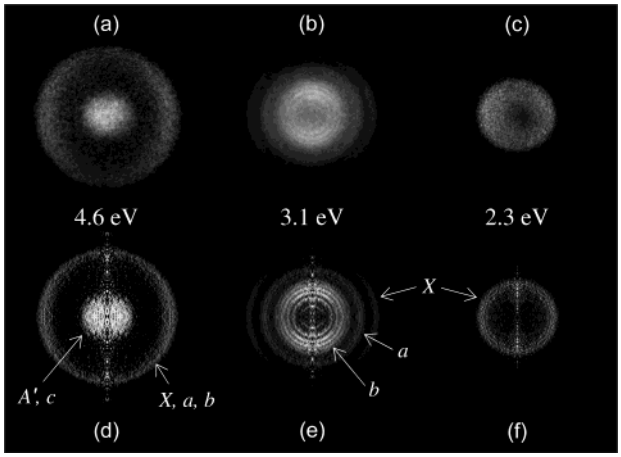


**Figure 3.** Top row: Photoelectron images recorded in the photodetachment of $S_2^-$ at (a) 267, (b) 400, and (c) 530 nm. Bottom row: Corresponding Abel inverted images, reconstructed as described in the text. The images are shown on arbitrary velocity and intensity scales; see Figures 7 and 8 for quantitative information. The laser polarization is always vertical in the figure plane. Arrows labeled *X*, *a*, *b*, *c*, and *A*′, indicate transitions assigned to the X $^3\Sigma_g^+$, a $^1\Delta$g, b $^1\Sigma_g^+$, c $^1\Sigma_u^-$, and A′ $^3\Delta_u$ states of $S_2$, respectively.

provided by a <25 ns rise/fall time pulse generator (Directed Energy PVM-4150), whose output is connected to the floated detector via a capacitor. The phosphor screen is monitored with a CCD camera (CoolSnap, Roper Scientific). The images are typically averaged for 10 000−30 000 experimental cycles and sent to the computer.

The laser radiation is generated using the amplified Ti: sapphire based laser system from Spectra Physics (1 mJ, 100 fs pulses). In the current work the 800 nm measurements use a portion (200−400 $\mu$J/pulse) of the unfocused fundamental output. The 530 nm radiation (30−50 $\mu$J/pulse) is generated by sum-frequency mixing the signal output of the optical parametric amplifier with the fundamental. The 400 nm light is generated by frequency-doubling a portion of the fundamental in a Super Tripler femtosecond harmonics generator (Super Optronics, Inc.), giving a 120 $\mu$J/pulse. The 267 nm light is also generated in the Super Tripler by mixing the fundamental and the second harmonic and giving 20 $\mu$J/pulse. The 530 and 400 nm beams are mildly focused with a 2 m focal-length lens, positioned 1.3 m before the interaction region. In all measurements, the polarization axis is parallel to the plane of the imaging detector.

## 3. Results and Analysis

The photoelectron images of $S_2^-$ and $CS_2^-$ are summarized in Figures 2 and 3, respectively. First, we give an overview of the analysis procedure that we apply to the images before proceeding to the discussion of the specific features of each anion. The top rows in Figures 2 and 3 depict the raw photoelectron images collected in the experiments, while the bottom rows display the corresponding Abel inverted images,[23] also referred to as reconstructed images. All images were obtained with the laser polarization set vertical in the image plane. Raw images are two-dimensional projections of the three-dimensional (3D) distributions of photoelectron velocity vectors, while the reconstructed images show the cross sections through the original 3D distributions in a plane containing the cylindrical symmetry axis, defined by the laser polarization direction.[23] These cross sections are obtained from the experimental images using the basis set expansion method developed by Reisler and co-workers.[9] The method uses a fitting procedure, which relies on the expansion of the raw image with a large basis set of functions that are the analytical Abel transforms of narrow Gaussian functions. The latter constitute the basis set for the reconstructed image.

In the images presented in Figures 2 and 3, electronic and in some cases vibrational transitions can be resolved. The imaging resolution is defined in absolute terms as $\Delta v$ in the velocity domain. Because of the eKE $\propto v^2$ scaling, the best energy resolution is achieved for the slowest electrons. Taking advantage of this feature, the photodetachment transitions to different neutral states can be brought into "focus" through changing the photon energy.

Photoelectron energy spectra and PADs are obtained by integrating the reconstructed images, including the necessary Jacobian factors.[23] The spectra are plotted versus electron binding energy eBE $= h\nu -$ eKE, allowing for direct comparison of the data obtained at different wavelengths. The PADs are extracted by integrating the signal intensity at a specific angle over the range of radii that encompass the ring (transition) of interest. The asymmetry parameter $\beta$ is determined by fitting the PADs using the expression for differential cross sections:[33]

$$d\sigma/d\Omega = (\sigma/4\pi)[1 + \beta P_2(\cos\theta)] \quad (1)$$

where $\theta$ is the angle between the laser polarization and the velocity vector of the ejected electron and $P_2(\cos\theta) = (3\cos^2\theta - 1)/2$ is a Legendre polynomial.

The following subsections detail the information contained within the $CS_2^-$ and $S_2^-$ photoelectron images.

**3.1. Photoelectron Images of $CS_2^-$.** An overview of the results for $CS_2^-$ is given in Figure 2. The images were obtained at 267, 400, 530, and 800 nm. The main features of the images shown in Figure 2b−d were briefly discussed in a previous communication.[13] $CS_2^-$ has a bent equilibrium geometry corresponding to the $^2A_1$ electronic state. At 400, 530, and 800 nm, only the transition to the ground X $^1\Sigma_g^+$ electronic state of $CS_2$ is energetically allowed. As the term symbol implies, this state has a linear equilibrium geometry; in the bent ($C_{2v}$) configuration accessed in vertical detachment the electronic

wave function symmetry corresponds to the $^1A_1$ state. In the MO picture, this transition involves the removal of the $a_1$ HOMO electron of $CS_2^-$.

In the 267 nm measurement, at least three additional electronic states of $CS_2$ are accessible, and hence several rings are easily discerned in the image shown in Figure 2a,e. The rings are labeled *X*, *a*, and *b*, corresponding to the X $^1\Sigma_g^+$, a $^3B_2$, and b $^3A_2$ states of neutral $CS_2$. Four electronic states of $CS_2$ have been seen previously by $CS_2^-$ photoelectron spectroscopy[51] that would be accessible at 267 nm. The fourth transition (to the A $^1A_2$ neutral state), which is not immediately apparent in the 267 nm image, is revealed in the analysis below.

Tuning the photon energy allows us to zoom in on the structure of different transitions, taking advantage of the higher energy resolution for slow electrons. For example, the dashed lines connecting Figure 2e and 2f, as well as Figure 2g and 2h, begin and end at the radial points corresponding to the same eBE for each pair of images. Therefore, these lines indicate the correlation of the chosen spectral intervals in the images taken at different photon energies. The image in Figure 2e ($h\nu = 4.6$ eV) emphasizes the higher energy transitions a and b, while the lower energy transition X is represented by a peripheral feature in which no structure can be discerned. The central area of the image in Figure 2e, including transitions a and b, corresponds to eBE > 3.1 eV. This entire energy range disappears in the 400 nm image shown in Figure 2f, while the range of eBE < 3.1 eV expands to the entire image area. This latter energy range includes only the electronic transition accessing the ground X $^1\Sigma_g^+$ state of $CS_2$. The vibrational structure of this transition becomes progressively better resolved as the photon energy is lowered further. The dashed lines between Figure 2g and 2h indicate the expansion of the radial range corresponding to eBE < 1.5 eV into the entire image area, as the laser is tuned to 800 nm. This final zoom reveals the rings corresponding to the transition's vibrational structure, as clearly seen in both the raw image in Figure 2d and the corresponding reconstructed image in Figure 2h.

As we discussed previously,[13] these rings correspond to the bending vibrational progression excited in the neutral core upon anion photodetachment. The progression originates from the vertical transition from the bent ground state of the anion to the highly excited bending vibrational levels of neutral $CS_2$, whose equilibrium geometry is linear.[49] The analysis of the 800 nm image[13] yields an average energy interval between the rings of 415 ± 10 $cm^{-1}$, consistent with the bending vibrational frequency in neutral $CS_2$.[49,59,60]

Even visual examination of the 800 nm images in Figure 2d,h reveals that the outer vibrational rings are more anisotropic than the inner ones. The values of the anisotropy parameter range from 0.37 to 0.78.[13] As discussed in section 4, the increase in $\beta$ with increasing eKE is attributed to the higher order partial waves competing with the isotropic s wave, which dominates near the detachment threshold.

Figure 4 shows an expanded version of the reconstructed 267 nm image from Figure 2e, superimposed with the eKE scale and neutral $CS_2$ state assignments for observed transitions. In this enlarged image, the A $^1A_2$ transition is discerned as an inner shadow of ring b. The observed transitions clearly exhibit different anisotropy properties. The 267 nm anisotropy parameters corresponding to the formation of the X $^1\Sigma_g^+$, $a^3B_2$, $b^3A_2$, and $A^1A_2$ neutral states are $\beta = 0.29$, $-0.24$, $-0.44$, and $-0.42$, respectively. Due to the overlap of the last three transitions, their $\beta$ values should be taken as estimates only.

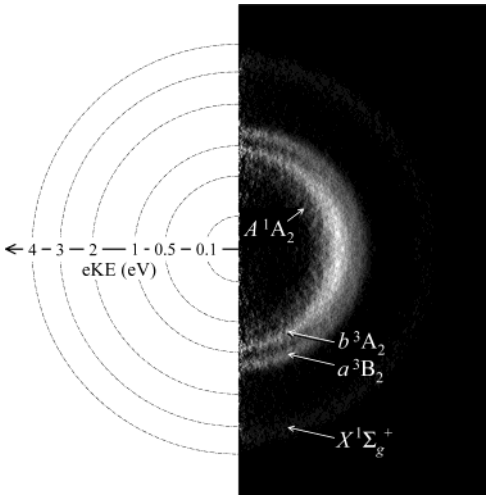


**Figure 4.** Half of the reconstructed 267 nm photoelectron image of $CS_2^-$ reproduced from Figure 2e (right) superimposed with the eKE scale (left) and neutral $CS_2$ state assignments for observed transitions.

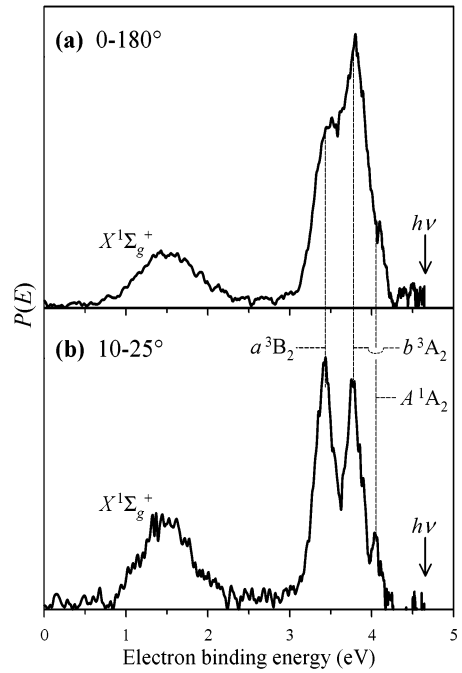


**Figure 5.** The 267 nm photoelectron spectrum of $CS_2^-$. (a) The spectrum obtained by integrating the reconstructed image in Figure 4 over the entire angular range. (b) The spectrum obtained by integrating the same image from $\theta = 10°$ to 25°. Peak assignments correspond to the electronic states of neutral $CS_2$.

The four transitions can also be seen in the photoelectron spectra shown in Figure 5. The spectrum in Figure 5a was obtained by integrating the image in Figure 4 over the entire angular range ($\theta = 0-180°$), while Figure 5b includes only a narrow sector $\theta = 10-25°$. The spectral peaks are labeled in accordance with the electronic states of $CS_2$ formed in the photodetachment, and the state assignments are taken from Tsukuda et al.[51] The three excited states of $CS_2$ overlap in Figure 5a, with a $^3B_2$ and A $^1A_2$ appearing as poorly resolved shoulders of the intense b $^3A_2$ peak. In the partially integrated spectrum in Figure 5b, the resolution is comparable to that achieved using traditional time-of-flight photoelectron spectroscopy,[51] with an added advantage of examining in detail the near zero eKE range. Restricting the angular integration range improves the resolution by minimizing the effects of distortions, such as possibly an

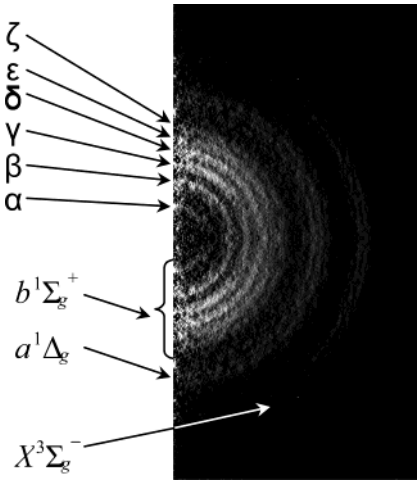


**Figure 6.** Expanded half of the reconstructed 400 nm photoelectron image of $S_2^-$ from Figure 3e. The electronic transition assignments correspond to neutral $S_2$ states formed in the detachment. The labels assigned to vibrational rings within the b $^1\Sigma_g^+$ transition are also shown.

imperfect roundness of the image and blurring due to a velocity spread in the ion beam. These effects are not observable by eye, but show up in the quantitative analysis.

In Figure 5b, the range of integration was chosen close to the laser polarization direction in order to reduce the relative intensity of the b $^3A_2$ peak, dominating the fully integrated spectrum in Figure 5a. Since the spectrum in Figure 5b does not account for all electrons produced in the photodetachment, the relative band intensities are not reflected properly.

**3.2. Photoelectron Images of $S_2^-$.** An overview of the $S_2^-$ results is presented in Figure 3. Using the assignments from Swope et al.,[61] the diffuse feature at the center of the 267 nm image (Figure 3a,d) is assigned to the transitions yielding the neutral c $^1\Sigma_u^-$ and/or A′ $^3\Delta_u$ states. This part of the image is nearly isotropic with $\beta \approx -0.14$. The outer ring in the 267 nm image is comprised of unresolved contributions of three electronic transitions: $^2\Pi_g \rightarrow$ X $^3\Sigma_g^-$, a $^1\Delta_g$, and b $^1\Sigma_g^+$. Changing the laser wavelength to 400 nm, we "zoom in" on these transitions and they become resolved in the image shown in Figure 3b,e. In the MO picture, each of these three transitions involves the removal of an electron from the doubly degenerate $\pi_g$* HOMO of $S_2^-$. Therefore, their comparative analysis is particularly instructive, as the observed anisotropy trends can be attributed to eKE-dependent photodetachment dynamics and/or deficiencies of the one-electron MO description.

The reconstructed 400 nm image from Figure 3e is enlarged in Figure 6. In this figure, vibrational rings are evident for all three electronic transitions, although they are best resolved for the slowest electrons, corresponding to the b $^1\Sigma_g^+$ neutral state. The electronic transitions are labeled in accordance with the resulting neutral states. Figure 7 shows the photoelectron spectra corresponding to the 400 and 530 nm $S_2^-$ images. Partial vibrational resolution is achieved for all three electronic transitions. The vibrational peaks for the b $^1\Sigma_g^+$ state transition are labeled using the assignments given to the corresponding rings in Figure 6. The peaks are spaced by $\sim$600 cm$^{-1}$, compared to the reported vibrational frequency for the b $^1\Sigma_g^+$ state of $S_2$, $\omega_e = 699.7$ cm$^{-1}$.[62] The discrepancy can be attributed, at least partially, to anharmonicity. The leading shoulder of the X band agrees with the known electron affinity (EA) of $S_2$ (1.670 $\pm$ 0.015 eV),[52] indicated by the dashed line in Figure 7. The signal at eBE < EA corresponds to hot bands and uncorrected backgrounds in the experimental image.

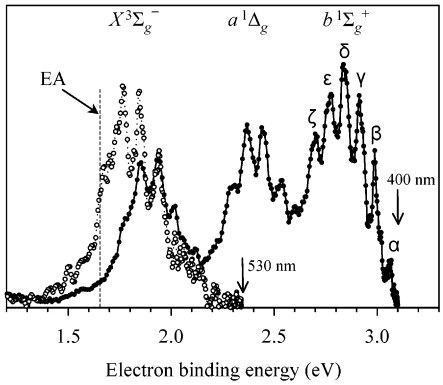


**Figure 7.** Photoelectron spectra of $S_2^-$ obtained from the images in Figure 3e,f. The spectrum represented by filled symbols/solid line corresponds to the 400 nm laser wavelength; open symbols/dotted line correspond to 530 nm. Vertical dashed line represents EA = 1.67 eV. The electronic state assignments correspond to neutral $S_2$. The vibrational progression (α through ζ) within the b state corresponds to the similarly labeled rings in the image shown in Figure 6.

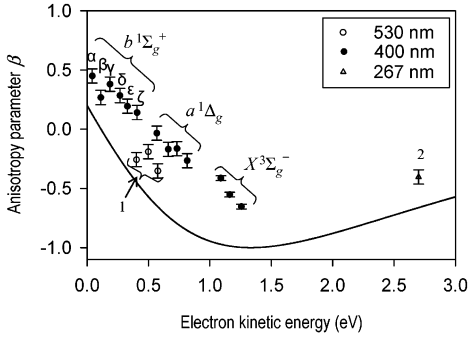


**Figure 8.** Anisotropy of different components of the $\pi_g^{-1}$ transition in $S_2^-$ at three different wavelengths (as indicated), summarized as a function of eKE. The transition labels indicated on the graph correspond to 400 nm data. The Greek labels for vibrationally resolved transitions to the b $^1\Sigma_g^+$ state of $S_2$ are the same as in Figures 6 and 7. (1) The 530 nm data corresponding to the X $^3\Sigma_g^-$ state. (2) Overall anisotropy of the peripheral feature in the 267 nm image shown in Figure 3a,d, corresponding to unresolved X $^3\Sigma_g^-$, a $^1\Delta_g$, and b $^1\Sigma_g^+$ states. The solid line corresponds to the Cooper−Zare model for photodetachment from a d orbital ($l = 2$) assuming a dipole radial matrix element ratio of $R_{l+1}/R_{l-1} = (0.5\ \text{eV}^{-1})$eKE and a zero phase shift between the ($l \pm 1$) waves. See the text for details.

Upon visual inspection of the 400 nm $S_2^-$ image in Figure 6, the inner part of the image corresponding to the transition to the b state is anisotropic with intensity peaking in the direction of the laser polarization, while the outer ring (X state transition) intensity maxima reside in the perpendicular direction. The middle ring, corresponding to the a state of $S_2$, appears nearly isotropic. The dependence of the anisotropy parameter on eKE is plotted in Figure 8. The $\beta$ values decrease with increasing eKE rather monotonically for all three transitions, following a common trend.

## 4. Discussion

The wave function of the free electron produced upon detachment from a bound orbital can be expanded in terms of partial waves characterized by definite values of the orbital angular momentum. For example, an electron detached from an atomic p orbital produces s and d waves, in accordance with the selection rule $\Delta l = \pm 1$. Near the detachment threshold, the cross section for each wave is well approximated by the Wigner law,[48] and thus the relative weight of the isotropic s wave is expected to be greater for slower electrons.[43] While the threshold

scaling of the cross section depends only on the $l$ quantum number, the corresponding PAD is dependent on both $l$ and $m_l$. For example, for p waves the angular distribution corresponding to a $p_z$ wave peaks along the $z$ axis, while any combination of $p_x$ and $p_y$ waves produces a peak in the direction perpendicular to $z$.

Molecular orbitals generally cannot be assigned a single $l$ value. As discussed by Reed et al.,[44] conceptually one can approach molecular detachment from two different viewpoints. We can choose to expand the parent MO ($\psi_{MO}$) as a linear combination of AO functions located at a single center in the MF. (Note that this differs from the LCAO−MO approach due to the single-center part.) Alternatively, we can use group theory and dipole selection rules to determine the symmetry of the free (photodetached) electron wave function ($\psi_f$) and then have *it* expanded in the symmetry-adapted single-center AO basis.

In the approach adopting the MO expansion, the Cooper−Zare central-potential model[33] can be applied to each $\psi_{MO}$ component to predict the energy-dependent anisotropy parameter $\beta$. The core approximation involved in the next step, which reduces the rigorous mathematical treatment[32] to a qualitative model, is the assumption that the basic character of molecular PADs can be determined without considering explicitly the interference of waves originating from different terms in the $\psi_{MO}$ expansion. This approach, to which we refer as the adapted Cooper−Zare treatment, works only when the $\psi_{MO}$ expansion in the single-center AO basis includes just a few (preferably one) dominant components.[45]

In the case of MOs with more complex structure, another qualitative approach is suggested. This method follows the formalism discussed by Reed et al. in the context of threshold photodetachment.[44] First, we use group theory to determine the free-electron wave function symmetry. Then, $\psi_f$ is expanded in terms of AO-type functions. The consideration is subsequently limited to only s and p partial waves, and therefore this approach is termed the s&p model.

Photodetachment of $S_2^-$ is an excellent candidate for the adapted Cooper−Zare treatment, with the core ideas used here having been applied previously to $O_2^-$ photodetachment.[18,40,46,47] The $\pi_g$ HOMO of $S_2^-$ has two nodal planes, making it very similar to an atomic d orbital. Hence, for the $\pi_g^{-1}$ transitions yielding the X $^3\Sigma_g^-$, a $^1\Delta_g$, and b $^1\Sigma_g^+$ neutral states, the initial orbital angular momentum quantum number of the electron can be taken as $l = 2$ and the trends in $\beta$ can be explained by considering the interference of the p and the f partial waves. In the case of $CS_2^-$, the MOs no longer resemble atomic orbitals; therefore, the s&p approach is applied for the qualitative interpretation of the PADs. Last, we consider the s&p treatment of $S_2^-$ and highlight the limitations of the model.

In the adapted Cooper−Zare treatment, the $S_2^-$ HOMO is approximated as an atomic d orbital, with p and f partial waves formed in the photodetachment. The Cooper−Zare formula[33] for $l = 2$ predicts that the asymmetry parameter will be positive at small eKEs, before reaching negative values. Figure 8 compares the experimental data for $S_2^-$ with the trend predicted by the Cooper−Zare central-potential model for detachment from a d orbital. The phase difference between the $(l \pm 1)$ partial waves was set to zero. Although this supposition is somewhat arbitrary, there is no physical basis for assuming a nonvanishing phase difference, at least in considering the qualitative trends in the detachment. In the relevant energy range the final-state de Broglie wavelength is quite large compared to the initial state and therefore no significant phase shift between the outgoing waves excited by the same laser field is expected.[43] Another model parameter, namely the ratio of the dipole radial matrix elements (affecting the position of the turnaround point on the curve), was chosen to simulate the trend in the data.

Although the experimental data in Figure 8 correspond to different wavelengths, as well as different final states, the anisotropy parameter appears to depend mainly on eKE, following a qualitative trend consistent with the Cooper−Zare model. This collective behavior is consistent with the MO picture, in which the X, a, and b neutral states are formed via different spin components of the same $\pi_g^{-1}$ one-electron detachment transition. Quantitative differences between the data and the model can be attributed, in part, to the neglected MO components, as well as electron interaction and intramolecular dynamics. In addition, the assumption of a central potential in the Cooper−Zare (atomic) model is less accurate in the case of the nonspherically symmetric molecular potential. Despite the quantitative discrepancies, this method is an effective qualitative tool for understanding the PAD's dependence on eKE.

A similar approach can be applied to electrons originating in orbitals below the HOMO. The A′ and c states of $S_2$ arise from detachment from the $\pi_u$ (HOMO − 1). Under symmetry restrictions, the lowest $l$ contributions to the single-center AO expansion of this MO correspond to p functions, followed by f functions, etc. If the AO expansion is dominated by the p functions, one expects them to yield s and d free-electron partial waves in the photodetachment. The s wave dominates at small eKEs, consistent with the nearly isotropic character of the observed PAD (see the central feature in the 267 nm images in Figure 3a,d), while the d wave contributes to the slightly negative $\beta$ ($-0.14 \pm 0.06$).

The MOs of $CS_2^-$ do not bear a convenient resemblance to atomic orbitals. Hence the expansion in AO functions will contain many nonnegligible terms, making the application of the adapted Cooper−Zare model rather cumbersome. In this case, it is more convenient to apply the s&p method, making use of the elements of the $C_{2v}$ point group to which $CS_2^-$ belongs. In the s&p model we first consider the detachment in the MF, requiring that the direct product of the irreducible representations of $\psi_{MO}$, $\psi_f$, and the dipole operator ($\mu$) is invariant under the symmetry operations of this group. After determining the allowed symmetries of the free-electron waves, $\psi_f$ can be expanded in a single-center AO basis. We then make a further approximation (best justified for slow electrons),[48] considering only the waves with $l \leq 1$. These s and p waves must then be referenced from the MF to the LF axes.

The LF PAD is determined by integrating over all molecular orientations. This is done accounting for the proportionality of transition amplitudes to the cosine of the angle between $\vec{\mu}$ and the laser polarization axis, defined to be the LF $z$ axis ($z_{LF}$). Qualitative insights into the nature of the PADs can be gained by considering only three "principal" orientations of the anion. These orientations are chosen so that one of the principal molecular axes is aligned along $z_{LF}$. This substitute for proper orientation averaging is, of course, a very coarse approximation, designed to give a qualitative picture of the detachment dynamics without embarking on complete quantum calculations.

The three principal orientations of $CS_2^-$ are shown schematically in the top row in Figure 9. For each orientation, only the transitions with nonzero $\vec{\mu}$ components along $z_{LF}$ are active. The symmetry species of the active dipole components with respect to the MF are indicated in the second header row in Figure 9. These symmetry species are the irreducible representations corresponding to $z_{LF}$ for the given MF orientations. Since only the irreducible representation of the $\vec{\mu}$ component along

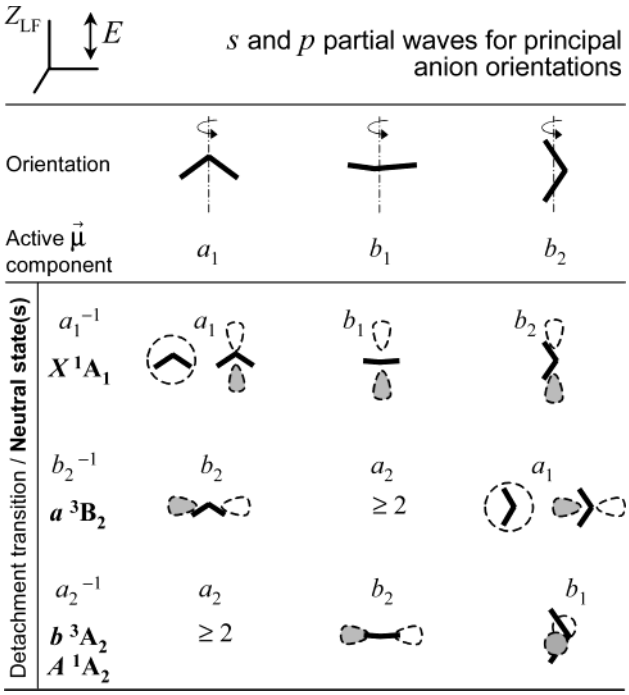


**Figure 9.** The s&p model treatment of $CS_2^-$ photodetachment. First header row: principal anion orientations (solid line represents the bent frame of $CS_2^-$). Second header row: corresponding symmetries of the transition-dipole components driven by the laser radiation polarized along the LF *z* axis. Rows below the header indicate the symmetries and s and p components (dash contours) of $\psi_f$ corresponding to the respective transitions and principal orientations. See the text for details.

$z_{LF}$ is important in the following discussion, all conclusions remain valid if the molecule is rotated about $z_{LF}$, as indicated in Figure 9, or inverted in the plane perpendicular to $z_{LF}$.

The MF symmetry of $\psi_f$ is determined by requiring $\langle \psi_f | \hat{\boldsymbol{\mu}} | \psi_{MO} \rangle \not\approx 0$. Photodetachment from the $a_1$ anion MO yields the X $^1A_1$ neutral state, while the $a_2^{-1}$ transition yields b $^3A_2$ or the A $^1A_2$. Similarly, the $b_2^{-1}$ yields both the $^3B_2$ and $^1B_2$ states, but only the triplet is observed due to the higher energy of $^1B_2$.[51] In Figure 9, the three rows below the header list the orientation-dependent $\psi_f$ symmetries allowed in the indicated transitions. For example, in the $b_2^{-1}$ transition, the free-electron waves detached from the anion orientations corresponding to the $a_1$, $b_1$, and $b_2$ active $\vec{\boldsymbol{\mu}}$ components are of $b_2$, $a_2$, and $a_1$ symmetries, respectively.

In the next step of the analysis, $\psi_f$ is expanded in a single-center AO basis, as done previously for the bound MOs. We then make a second core approximation, limiting the consideration to s and p partial waves only. An s wave always corresponds to the $a_1$ representation, but p waves can transform as $a_1$, $b_1$, or $b_2$ symmetry species, depending on the wave polarization in the MF. The dashed contours in Figure 9 show schematically the s and p components of $\psi_f$ under the symmetry constraints determined above.

If $\psi_f$ transforms as $a_1$, the ejected electron can have both s and p partial components. While the s waves are isotropic, the LF orientation of the p waves is determined by their MF symmetry and the anion orientation being considered. For $\psi_f$ of $b_1$ and $b_2$ symmetries, only p-wave components are considered in the model. For $a_2$ waves, the smallest $l$ components correspond to d orbitals; therefore, $a_2$ waves are neglected under the $l \leq 1$ approximation.

Considering the wave sketches in Figure 9, the qualitative nature of the expected PADs becomes immediately clear. For the $a_1^{-1}$ (X $^1A_1$) transition, the free-electron wave function is characterized by interference of the isotropic s waves and anisotropic p waves with amplitudes peaking along $z_{LF}$. Thus, a PAD with positive $\beta$ is expected, in agreement with the experimental results. For example, the 800 nm PAD for the X $^1A_1$ transition integrated over all eKEs is characterized by $\beta = 0.68$. Similar values are obtained at 530 and 400 nm.[13] The eKE dependence of the anisotropy of the vibrational rings in Figure 2d,h can also be understood qualitatively using the s&p analysis. Compared to the s waves, the p-wave amplitude is small for slow electrons, increasing with increasing eKE (Wigner law). Therefore, the anisotropy for this transition should increase with increasing eKE. This predicted behavior can be seen in the 800 nm data (see Figure 2h).

For the $b_2^{-1}$ (a $^3B_2$) transition, the s&p model predicts two principal p waves with amplitudes peaking in the direction perpendicular to the laser polarization, as well as an isotropic s wave. Thus, $\beta < 0$ is expected, as is indeed observed in the experiment (see Figure 4).

For the $a_2^{-1}$ (b $^3A_2$ and A $^1A_2$) transition, $l = 0$ components of $\psi_f$ are forbidden in the electric-dipole approximation. As indicated in Figure 9, only horizontally polarized p waves are produced in the detachment under the approximations of the s&p model. A substantially negative value of $\beta$ is therefore predicted for these transitions.

In the above two cases ($b_2^{-1}$ and $a_2^{-1}$ transitions) $\beta < 0$ is expected. However, in the latter case, only p waves polarized perpendicular to $z_{LF}$ are predicted for the principal orientations within the approximations of the model, while for the $b_2^{-1}$ transition similar p waves are predicted to compete with an s component, which can be particularly intense for slow electrons. Thus, another qualitative prediction can be drawn from these arguments: the perpendicular nature of the anisotropy is expected to be more pronounced in the "pure p" case of the $a_2^{-1}$ transition than in the "mixed s and p" case of the $b_2^{-1}$ transition. That this prediction is also confirmed by the experiment is easily seen in the 267 nm photoelectron image in Figure 2a and its Abel transform in Figure 4: the $a_2^{-1}$ transition does indeed exhibit a more negative anisotropy ($\beta = -0.44$ and $-0.42$ for b $^3A_2$ and A $^1A_2$, respectively) than the $b_2^{-1}$ transition ($\beta = -0.24$ for a $^3B_2$).

The application of the s&p model to $CS_2^-$ photodetachment makes use of the specific properties of the $C_{2v}$ point group. Nonetheless, the same general approach can be applied to other molecular anions, such as, for example, $S_2^-$. In this case, the model can be compared to the Cooper−Zare method adapted to the molecular case as described above. Although the application of the Cooper−Zare method to $S_2^-$ is straightforward, in our view the s&p model has an important pedagogical advantage, as long as the detachment is considered in a qualitative manner only. We refer, of course, to the ease of visualization, which contrasts the s&p model with the Cooper−Zare formalism.[33]

Following the s&p approach, Figure 10 shows the sketches of $l < 2$ partial waves allowed in the detachment from the $\pi_g$ HOMO of $S_2^-$ in the three principal orientations of the anion frame. The first orientation (Figure 10, top) corresponds to a $\sigma_u^+(\mu_z)$ active dipole component and yields waves of $\pi_u$ symmetry. The second and third principal orientations are characterized by the degenerate $\pi_u$ active components of the transition dipole. The $\mu_x$ component yields free-electron waves of $\sigma_u^+$ symmetry (Figure 10, middle), while $\mu_y$ produces $\sigma_u^-$ and $\delta_u$ waves (Figure 10, bottom). Involving the AO basis expansion and the $l < 2$ model approximation, only the p free-electron waves indicated in the right column of Figure 10 are

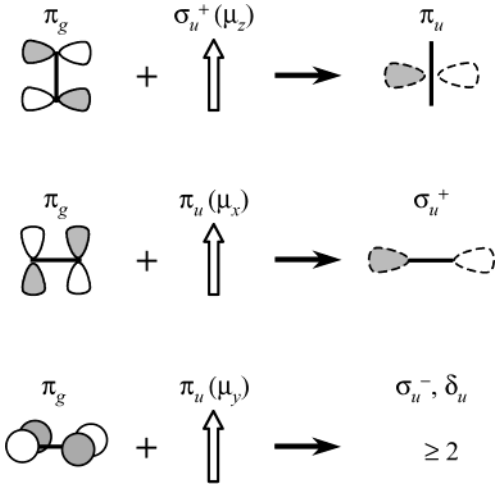


**Figure 10.** The s&p model treatment of $S_2^-$ ($\pi_g^{-1}$) photodetachment. Bold solid line is the S−S internuclear axis molecular frame. Solid contours on the left represent the bound MO ($\pi_g$). Vertical arrows in the middle indicate the laser polarization direction, with the corresponding MF symmetry of the active transition dipole components shown. Dashed contours on the right represent the symmetry-allowed partial waves ($l \leq 1$) that contribute to $\psi_f$. The $\sigma_u^-$ and $\delta_u$ waves corresponding to the $\pi_u(\mu_y)$ transition moment expands only in $l \geq 2$ waves, which are neglected in the model.

considered. These waves are polarized perpendicular to the laser polarization axis, and hence $\beta < 0$ is predicted.

Thus, the s&p model predicts $\beta < 0$ for all three $\pi_g^{-1}$ transitions yielding the X $^3\Sigma_g^-$, a $^1\Delta g$, and b $^1\Sigma_g^+$ neutral states. The 400 nm experiment shows that $\beta$ is indeed substantially negative for the X state ($\beta = -0.54 \pm 0.02$, integrated over all vibrational components). However, the overall anisotropies are almost zero ($\beta = -0.16 \pm 0.06$) and even positive ($\beta = 0.29 \pm 0.06$) for the a and b states, respectively. Although the $\beta$ values for the a and b states tend to become negative as eKE increases, this case highlights the limitations of the model inherent in its qualitative nature. The Cooper−Zare wave composition depends on the initial state orbital angular momentum, while the s&p model in its present formulation always includes only s and p waves. (However, some generalization of the model to include higher order waves is in principle possible.) As a consequence of this limitation, only p-wave contributions are considered in the photodetachment of $S_2^-$. Thus, the s&p model may serve as an insightful tool for determining the overall nature of the detachment process, as reflected in its anisotropy at intermediate eKEs, while predicting the anisotropy at any given eKE requires a more rigorous, quantitative approach.

For the transitions arising from the $\pi_u$ (HOMO − 1) of $S_2^-$, the allowed partial waves are $\sigma_g^+$, $\sigma_g^-$, $\delta_g$, and $\pi_g$. Of these, only the $\sigma_g^+$ wave contains partial waves with $l < 2$, namely, the isotropic s functions. All other waves formed under the above symmetry restrictions expand in $l \geq 2$ AO functions. Thus, p waves are forbidden for this transition under the one-electron, electric-dipole approximations. The s partial wave is responsible for a nearly isotropic PAD predicted for this case, in agreement with the nearly isotropic ($\beta = -0.14 \pm 0.06$) A′, c feature in Figure 3a,d.

## 5. Summary

We have discussed the utility of photoelectron imaging in probing the electronic structure of small molecular anions. The results for two model systems, $S_2^-$ and $CS_2^-$, have been presented. For both anions, photoelectron images recorded at a series of wavelengths have been used to examine the electronic structure and the electron ejection dynamics.

Two qualitative approaches to describing the detachment processes and resulting PADs have been discussed. The objective of these models is to provide basic understanding and tutorial description of electron detachment dynamics without invoking full-scale quantum calculations. The $S_2^-$ and $CS_2^-$ results have been used to illustrate the two approaches.

The first model is an extension of the central-potential model of Cooper and Zare for atomic ionization and photodetachment.[33] Formally, this model considers an expansion of the MO in the basis of single-center AO functions, for which the partial waves of the ejected electron can be determined. The generalization of this model for the molecular anion case is practical only if the parent MO resembles an atomic orbital, which is the case for $S_2^-$, but not $CS_2^-$.

For photodetachment from MOs that cannot be conveniently approximated by a single AO (e.g., $CS_2^-$), the qualitative s&p model was suggested, which restricts the analysis to s and p partial waves and treats the orientation averaging by considering only a few "principal" molecular orientations.

It is hoped that these results will provide a tutorial foundation for the qualitative interpretation of anion photoelectron images, which will be useful in developing more sophisticated approaches to more complex systems.

**Acknowledgment.** We thank V. Dribinski and Professor H. Reisler for providing the image analysis software. Discussions with Professors W. C. Lineberger and H. Reisler are gratefully acknowledged. This work is supported by the NSF Grants CHE-9982057 and CHE-0134631, the Beckman Young Investigator Award, ACS PRF Grant 35589-G6, and the Research Corporation Research Innovation Award No. RI0515. A.S. is a 2002 Packard Foundation Fellow.

## References and Notes

(1) Lochbrunner, S.; Larsen, J. J.; Shaffer, J. P.; Schmitt, M.; Schultz, T.; Underwood, J. G.; Stolow, A. *J. Electron Spectrosc. Relat. Phenom.* **2000**, *112*, 183.
(2) Davies, J. A.; LeClaire, J. E.; Continetti, R. E.; Hayden, C. C. *J. Chem. Phys.* **1999**, *111*, 1.
(3) Davies, J. A.; Continetti, R. E.; Chandler, D. W.; Hayden, C. C. *Phys. Rev. Lett.* **2000**, *84*, 5983.
(4) Wang, L.; Kohguchi, H.; Suzuki, T. *Faraday Discuss.* **1999**, *113*, 37.
(5) Suzuki, T.; Wang, L.; Kohguchi, H. *J. Chem. Phys.* **1999**, *111*, 4859.
(6) Chandler, D. W.; Houston, P. L. *J. Chem. Phys.* **1987**, *87*, 1445.
(7) Eppink, A. T. J. B.; Parker, D. H. *Rev. Sci. Instrum.* **1997**, *68*, 3477.
(8) Parker, D. H.; Eppink, A. T. J. B. *J. Chem. Phys.* **1997**, *107*, 2357.
(9) Dribinski, V.; Ossadtchi, A.; Mandelshtam, V. A.; Reisler, H. *Rev. Sci. Instrum.* **2002**, *73*, 2634.
(10) Chang, B. Y.; Hoetzlein, R. C.; Mueller, J. A.; Geiser, J. D.; Houston, P. L. *Rev. Sci. Instrum.* **1998**, *69*, 1665.
(11) Rogers, L. J.; Ashfold, M. N. R.; Matsumi, Y.; Kawasaki, M.; Whitaker, B. J. *Chem. Phys. Lett.* **1996**, *258*, 159.
(12) Deyerl, H. J.; Alconcel, L. S.; Continetti, R. E. *J. Phys. Chem. A* **2001**, *105*, 552.
(13) Surber, E.; Sanov, A. *J. Chem. Phys.* **2002**, *116*, 5921.
(14) Zare, R. N. *Mol. Photochem.* **1972**, *4*, 1.
(15) Houston, P. L. *Acc. Chem. Res.* **1995**, *28*, 453.
(16) Demyanenko, A. V.; Potter, A. B.; Dribinski, V.; Reisler, H. *J. Chem. Phys.* **2002**, *117*, 2568.
(17) Demyanenko, A. V.; Dribinski, V.; Reisler, H.; Meyer, H.; Qian, C. X. W. *J. Chem. Phys.* **1999**, *111*, 7383.
(18) Sherwood, C. R.; Garner, M. C.; Hanold, K. A.; Strong, K. M.; Continetti, R. E. *J. Chem. Phys.* **1995**, *102*, 6949.
(19) Dehmer, J. L.; Dill, D. *Phys. Rev. A* **1978**, *18*, 164.
(20) Wallace, S.; Dill, D. *Phys. Rev. B* **1978**, *17*, 1692.
(21) Jonah, C. *J. Chem. Phys.* **1971**, *55*, 1915.
(22) Busch, G. E.; Wilson, K. R. *J. Chem. Phys.* **1972**, *56*, 3638.

(23) Heck, A. J. R.; Chandler, D. W. *Annu. Rev. Phys. Chem.* **1995**, *46*, 335.
(24) Sanov, A.; Droz-Georget, T.; Zyrianov, M.; Reisler, H. *J. Chem. Phys.* **1997**, *106*, 7013.
(25) Baguenard, B.; Pinare, J. C.; Bordas, C.; Broyer, M. *Phys. Rev. A* **2001**, *63*, 23204.
(26) Pinare, J. C.; Baguenard, B.; Bordas, C.; Broyer, M. *Eur. Phys. J. D* **1999**, *9*, 21.
(27) Baguenard, B.; Pinare, J. C.; Lepine, F.; Bordas, C.; Broyer, M. *Chem. Phys. Lett.* **2002**, *352*, 147.
(28) Surber, E.; Sanov, A. *Phys. Rev. Lett.* **2003**, *90*, 93001.
(29) Seideman, T. *J. Chem. Phys.* **1997**, *107*, 7859.
(30) Hanold, K. A.; Garner, M. C.; Continetti, R. E. *Phys. Rev. Lett.* **1996**, *77*, 3335.
(31) Continetti, R. E. *Annu. Rev. Phys. Chem.* **2001**, *52*, 165.
(32) Cooper, J.; Zare, R. N. Photoelectron angular distributions. In *Atomic collision processes*; Geltman, S., Mahanthappa, K. T., Brittin, W. E., Eds.; Gordon and Breach Science Publishers: New York, London, Paris, 1968; Vol. XI-C, p 317.
(33) Cooper, J.; Zare, R. N. *J. Chem. Phys.* **1968**, *48*, 942. Cooper, J.; Zare, R. N. *J. Chem. Phys.* **1968**, *49*, 4252.
(34) Tully, J. C.; Berry, R. S.; Dalton, B. J. *Phys. Rev.* **1968**, *176*, 95.
(35) Park, H.; Zare, R. N. *J. Chem. Phys.* **1996**, *104*, 4554.
(36) Park, H.; Zare, R. N. *J. Chem. Phys.* **1996**, *104*, 4568.
(37) Seideman, T. *J. Chem. Phys.* **2000**, *113*, 1677.
(38) Seideman, T. *Phys. Rev. A* **2001**, *64*, 42504.
(39) Seideman, T. *Annu. Rev. Phys. Chem.* **2002**, *53*, 41.
(40) Lin, P.; Lucchese, R. R. *J. Chem. Phys.* **2001**, *114*, 9350.
(41) Mead, R. D.; Lykke, K. R.; Lineberger, W. C. Photodetachment Threshold Laws. In *Electronic and Atomic Collisions*; Eichler, J., Hertel, I. V., Stolterfoht, N., Eds.; Elsevier: New York, 1984; p 721.
(42) Hall, J. L.; Siegel, M. W. *J. Chem. Phys.* **1968**, *48*, 943.
(43) Hanstorp, D.; Bengtsson, C.; Larson, D. J. *Phys. Rev. A* **1989**, *40*, 670.
(44) Reed, K. J.; Zimmerman, A. H.; Andersen, H. C.; Brauman, J. I. *J. Chem. Phys.* **1976**, *64*, 1368.
(45) Gilles, M. K.; Ervin, K. M.; Ho, J.; Lineberger, W. C. *J. Phys. Chem.* **1992**, *96*, 1130.
(46) Celotta, R. J.; Bennett, R. A.; Levine, J.; Hall, J. L.; Siegel, M. W. *Phys. Rev. A* **1972**, *6*, 631.
(47) Burch, D. S.; Smith, S. J.; Branscomb, L. M. *Phys. Rev.* **1958**, *112*, 171.
(48) Wigner, E. P. *Phys. Rev.* **1948**, *73*, 1002.
(49) Oakes, J. M.; Ellison, G. B. *Tetrahedron* **1986**, *42*, 6263.
(50) Bowen, K. H.; Eaton, J. G. Photodetachment Spectroscopy of Negative Cluster Ions. In *The Structure of Small Molecules and Ions*; Naaman, R., Vager, Z., Eds.; Plenum: New York, 1988; p 147.
(51) Tsukuda, T.; Hirose, T.; Nagata, T. *Chem. Phys. Lett.* **1997**, *279*, 179.
(52) Moran, S.; Ellison, G. B. *J. Phys. Chem.* **1988**, *92*, 1794.
(53) Johnson, M. A.; Lineberger, W. C. Pulsed Methods for Cluster Ion Spectroscopy. In *Techniques for the Study of Ion Molecule Reactions*; Farrar, J. M., Saunders, W. H., Eds.; Wiley: New York, 1988; p 591.
(54) Wiley, W. C.; McLaren, I. H. *Rev. Sci. Instrum.* **1955**, *26*, 1150.
(55) Surber, E.; Ananthavel, S. P.; Sanov, A. *J. Chem. Phys.* **2002**, *116*, 1920.
(56) Nadal, M. E.; Kleiber, P. D.; Lineberger, W. C. *J. Chem. Phys.* **1996**, *105*, 504.
(57) Posey, L. A.; Deluca, M. J.; Johnson, M. A. *Chem. Phys. Lett.* **1986**, *131*, 170.
(58) Mabbs, R.; Surber, E.; Sanov, A. *Analyst* **2003**, *128*, in press.
(59) Suzuki, I. *Bull. Chem. Soc. Jpn.* **1975**, *48*, 1685.
(60) Gutsev, G. L.; Bartlett, R. J.; Compton, R. N. *J. Chem. Phys.* **1998**, *108*, 6756.
(61) Swope, W. C.; Lee, Y.-P.; Schaefer, H. F., III. *J. Chem. Phys.* **1979**, *70*, 947.
(62) Chemistry WebBook—NIST Standard Reference Database; No. 69 (July 2001 release).